Journal of Zhejiang University-SCIENCE A (Applied Physics & Engineering)
ISSN 1673-565X (Print); ISSN 1862-1775 (Online)
www.jzus.zju.edu.cn; www.springerlink.com
E-mail: jzus@zju.edu.cn

A dynamic constitutive model of ultra high toughness cementitious composites*

Shi-lang XU, Ping WU, Fei ZHOU, Xiao JIANG, Bo-kun CHEN, Qing-hua LI†‡

Institute of Advanced Engineering Structures and Materials, Zhejiang University, Hangzhou 310058, China

†E-mail: liqinghua@zju.edu.cn

Received Nov. 24, 2019; Revision accepted July 1, 2020; Crosschecked Nov. 16, 2020

Abstract: In this study, an explicit dynamic constitutive model was established for ultra high toughness cementitious composites (UHTCCs). The model, based on the Holmquist–Johnson–Cook (HJC) model, includes tensile and compressive damage evolution, hydrostatic pressure, strain rate, and the Lode angle effect. The proposed model was embedded in LS-DYNA software and then comprehensive tests were carried on a hexahedral brick element formulation under uniaxial, biaxial, and triaxial stress states to verify its rationality through comparisons with results determined by the HJC and Karagozian & Case (K&C) models. Finally, the proposed model was used to simulate the damage caused to UHTCC targets subjected to blast by embedded explosive and projectile penetration, and predictions were compared with corresponding experimental results. The results of the numerical simulations showed that our proposed model was more accurate than the HJC model in predicting the size of the crater, penetration depth, and the distribution of cracks inside the target following the blast or high-speed impact loading.

Key words: Holmquist–Johnson–Cook (HJC) model; Ultra high toughness cementitious composite (UHTCC); Constitutive model; Explosion test; Projectile penetration; Numerical simulation

https://doi.org/10.1631/jzus.A1900599 **CLC number:** TU501

1 Introduction

Ultra high toughness cementitious composites (UHTCCs) are highly ductile and tough materials. When subjected to tensile loads, these materials exhibit ultimate tensile strains greater than 3%, resulting in a large number of micro-cracks rather than large fractures (Xu and Cai, 2008; Xu and Li, 2010). Therefore, UHTCCs significantly reduce the brittleness of conventional concrete materials when subjected to tensile loads. In drop hammer tests, Liu (2012) showed that the impact energy dissipation of UHTCCs is 48 times higher than that of ordinary concrete and 9 times higher than that of steel fiber-reinforced concrete. Soe et al. (2013) performed high-velocity impact tests on engineered cementitious composite (ECC) panels containing polyvinyl alcohol (PVA) fibers, and found that they outperformed conventional concrete panels in terms of the diameter of the impact crater, integrity, and fragmentation. These results demonstrated that UHTCCs have a wide range of potential applications in protective engineering. However, if they are to be applied as key components in engineering designs, it is necessary to understand the mechanical responses of UHTCC structures subjected to dynamic loads.

Although the dynamic tensile behaviors (Li and Xu, 2016), dynamic compressive behaviors (Li et al., 2016a), uniaxial fatigue performance, and crack propagation behaviors (Li et al., 2016b) of UHTCCs have been studied experimentally by researchers

‡ Corresponding author

* Project supported by the National Natural Science Foundation of China (Nos. 51678522 and 51878601)

ORCID: Qing-hua LI, https://orcid.org/0000-0003-2694-1936

around the world, experimental data and guiding principles on the application of such materials to protective engineering are still lacking. Furthermore, high-velocity impact tests and explosive load tests on UHTCC structures are very expensive and time consuming, and the use of the data produced by these tests is rather limited. Computer horsepower and constitutive concrete models have been around for decades, and have made it possible to predict the failure modes of UHTCC structures effectively via numerical simulations. However, systematic studies focusing on the dynamic constitutive relations of UHTCCs are still lacking. The response of such materials to dynamic loads is still being used in ordinary concrete constitutive models, such as the Holmquist–Johnson–Cook (HJC) model (Holmquist et al., 1993), Riedel–Hiermaier–Thoma (RHT) model (Riedel et al., 1999), Karagozian & Case (K&C) model (Malvar et al., 1997), and the continues surface cap model (CSCM) (Murray, 2007). However, the ability of these models to describe the dynamic properties of UHTCCs is somewhat limited. Therefore, the development of a dynamic constitutive model suitable for UHTCCs is of utmost importance.

Holmquist, Johnson, and Cook developed the HJC model based on an extension of the Johnson–Cook model for metals (Johnson and Cook, 1983). They used this model to simulate high-speed impacts by ogive-nose projectiles on concrete panels, and thereby obtained residual projectile velocities that were consistent with experimental data. However, the HJC model did not account for the effects of the Lode angle, nor did it consider tensile damage. Consequently, it did not provide information about impact-induced cratering, crack propagation, and void collapse. Researchers attempted to address these flaws by modifying the HJC model. In the modified HJC model of Polanco-Loria et al. (2008), the influence of the third deviatoric stress invariant was taken into account, and the modeling of the failure surface and strain rate sensitivity was amended. This modified model was used to simulate the perforation of 48-MPa and 140-MPa concrete slabs by projectiles, and the damage to the concrete slabs was illustrated using contour maps. Based on the extended Drucker–Prager strength criterion and the HJC model, Li and Shi (2016) constructed a dynamic constitutive model for rock materials that defined tensile damage in terms of volumetric strain, and accounted for the effects of the third deviatoric stress invariant on the yield surface. This model was used successfully to simulate the impact of ogive-nose projectiles on granite targets. Liu et al. (2009) combined the tension component of the Taylor–Chen–Kuszmaul (TCK) continuum damage model with the compression component of the HJC model, and used the resulting model to simulate the penetration of concrete targets by deformable projectiles at oblique angles. Although this model successfully reproduced the cratering response of the concrete targets, it had a discontinuous failure surface at zero hydrostatic pressure. Kong et al. (2016) comprehensively modified the HJC model based on the incorporation of the effects of the Lode angle and tensile damage. Accordingly, the scabbing and cratering predicted by this model in concrete targets were in excellent agreement with the experimental data.

In this study, based on the modified HJC model and currently available experimental data, a dynamic constitutive model that specifically describes the ductile behavior of UHTCCs under tension was established. In this model, a tensile damage function was introduced to reflect the ductility and softening behaviors of UHTCCs, a smooth, continuous, and convex-shaped failure surface that accounts for the effects of the Lode angle was developed, and the equations describing strain rate and compressive softening behaviors in the HJC model were modified. Furthermore, the volumetric damage caused by triaxial tension and compression was included in the model. The new material model was then implemented in LS-DYNA as a user-material model to simulate UHTCC targets under blast and high-speed impact loading. The effectiveness and accuracy of our new model were validated against experimental results. This study provides scientific evidence supporting the practical application of UHTCCs in protective engineering.

2 Constitutive model

2.1 Yield surface equations

The yield surface equations of the HJC model are manifested in the form of pressure, damage, and strain rate functions:

$$\sigma_{\mathrm{eq}}^{*}=\begin{cases}A\left(\dfrac{P^{*}}{T^{*}}+1-D\right)(1+C\ln\dot{\varepsilon}^{*}), & P^{*}<0,\\ \left[A(1-D)+BP^{*N}\right](1+C\ln\dot{\varepsilon}^{*})\le S_{\max}, & P^{*}\ge 0,\end{cases} \tag{1}$$

where $\sigma_{\mathrm{eq}}^{*}=\sigma/f_{\mathrm{c}}$, σ is the real effective strength, and f_{c} is the uniaxial compressive strength of the concrete. $P^{*}=P/f_{\mathrm{c}}$ is the dimensionless hydrostatic pressure, and P is the hydrostatic pressure. $T^{*}=T/f_{\mathrm{c}}$ is the dimensionless uniaxial tensile strength, and T is the uniaxial tensile strength. $\dot{\varepsilon}^{*}=\dot{\varepsilon}/\dot{\varepsilon}_{0}$ is the dimensionless strain rate, $\dot{\varepsilon}$ is the strain rate, and $\dot{\varepsilon}_{0}$ is the reference strain rate. The constants A, B, N, and C are determined based on testing of concrete material. D is the damage parameter, and $S_{\max}$ is the dimensionless maximum strength.

The damage parameter D represents the amount of damage in the concrete material. The effects of shear damage and compressive damage on the strength of a concrete material are given by D in the HJC model, whose mathematical expression is

$$D=\sum\frac{\Delta\varepsilon_{\mathrm{p}}+\Delta\mu_{\mathrm{p}}}{\varepsilon_{\mathrm{p}}^{\mathrm{f}}+\mu_{\mathrm{p}}^{\mathrm{f}}},\qquad \varepsilon_{\mathrm{p}}^{\mathrm{f}}+\mu_{\mathrm{p}}^{\mathrm{f}}=D_{1}(P^{*}+T^{*})^{D_{2}}\ge\varepsilon_{\mathrm{fmin}}, \tag{2}$$

where $\Delta\varepsilon_{\mathrm{p}}$ is the equivalent plastic strain increment, $\Delta\mu_{\mathrm{p}}$ is the volumetric plastic strain increment, $\varepsilon_{\mathrm{p}}^{\mathrm{f}}+\mu_{\mathrm{p}}^{\mathrm{f}}$ is the plastic strain when the concrete material fractures, and $\varepsilon_{\mathrm{fmin}}$ is the amount of plastic strain before fracture. D_1 and D_2 are constants.

The HJC model does not consider the effects of the third deviatoric stress invariant on the yield surface or tensile damage. Furthermore, it uses a unified strain rate equation to describe tensile extension and compression, but it has been demonstrated experimentally that the effects of the tensile strain rate are much more significant than those of the compressive strain rate (Kong et al., 2016). To address these issues, Xu and Wen (2016) developed a new equation for the yield strength of concrete materials that divides the failure surface into three regions. Using their modified model, they successfully simulated the mechanical response of concrete subjected to dynamic loads. Based on their work, taking tensile and compressive damage into consideration, an equation is proposed to describe the continuous, convex-shaped, and smooth failure surface:

$$\sigma_{\mathrm{eq}}^{*}=\begin{cases}\left[3\left(P+f_{\mathrm{tt}}\right)\right]r', & P\le 0,\\ \left[3\left(P+f_{\mathrm{tt}}\right)+\alpha\left(\dfrac{P}{f_{\mathrm{c}}}\right)^{2}+\beta\left(\dfrac{P}{f_{\mathrm{c}}}\right)^{3}\right]r', & 0<P\le\dfrac{f_{\mathrm{cc}}}{3},\\ \left[f_{\mathrm{cc}}-Bf_{\mathrm{c}}\left(\dfrac{1}{3}\right)^{N}+Bf_{\mathrm{c}}\left(\dfrac{P}{f_{\mathrm{c}}}\right)^{N}\right]r', & P\ge\dfrac{f_{\mathrm{cc}}}{3},\end{cases} \tag{3}$$

where r' is the ratio of the current meridian to the compression meridian. $f_{\mathrm{cc}}=\max(f_{\mathrm{c}}(1-D_{\mathrm{c}}), 0.3f_{\mathrm{c}})$ controls the compression softening and the residual strength, and D_{c} is the compression damage. $f_{\mathrm{tt}}=T(1-D_{\mathrm{t}})$ controls the tensile softening, and D_{t} is the tensile damage. α and β are coefficients. B and N are fitted from the data of triaxial compression tests.

The strength of the yield surface, σ_{eq}^{*}, under hydrostatic loading can be obtained from triaxial tests. Some of the published results of triaxial (Li et al., 2010; Wen, 2015; Ren et al., 2016; Khan et al., 2018) and biaxial (Zhou et al., 2013; Pan et al., 2016) compression tests are shown in Fig. 1. The parameters of the compressive meridian are thus B=1.8 and N=0.8, and the values of α and β can be obtained from the smooth and continuous line at $P=f_{\mathrm{cc}}/3$ on the yield surface, which are given by Eqs. (4) and (5). Finally, the tensile meridian can be obtained based on the tensile meridian ratio.

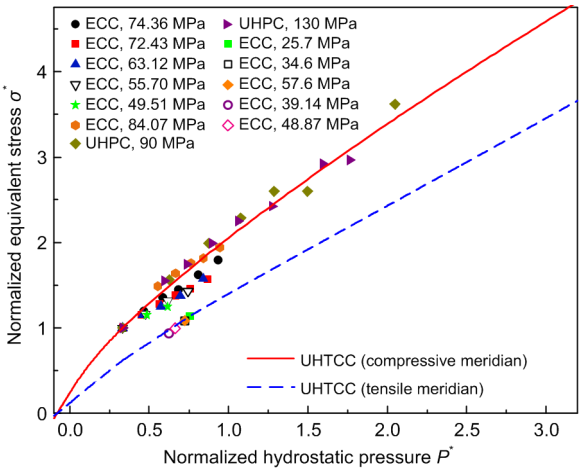

Fig. 1 UHTCC triaxial confining pressure and biaxial compression test data (UHPC denotes ultra high performance concrete)

$$\alpha=\frac{9\left(\frac{f_{cc}}{f_c}\right)-81\left(\frac{f_{tt}}{f_c}\right)-3BN\left(\frac{f_{cc}}{f_c}\right)\left(\frac{f_{cc}}{3f_c}\right)^{N-1}}{\left(\frac{f_{cc}}{f_c}\right)^2}, \quad (4)$$

$$\beta=\frac{-27\left(\frac{f_{cc}}{f_c}\right)+162\left(\frac{f_{tt}}{f_c}\right)+9BN\left(\frac{f_{cc}}{f_c}\right)\left(\frac{f_{cc}}{3f_c}\right)^{N-1}}{\left(\frac{f_{cc}}{f_c}\right)^3}. \quad (5)$$

2.2 Lode angle effects

The shape of the yield surface in the deviatoric plane has a considerable effect on the outcome of numerical simulations on UHTCC materials. To describe the transition of the deviatoric plane from a near-triangular shape at low-hydrostatic pressures to a near-circular shape at high-hydrostatic pressures (Fig. 2), our new model must account for the effects of the third deviatoric stress invariant, that is, the Lode angle. Willam and Warnke (1975) proposed a smooth, convex, and triangular yield surface that accounts for the Lode angle, as follows:

$$r'(\theta,\varphi)=\frac{2\left(1-\varphi^2\right)\cos\theta}{4\left(1-\varphi^2\right)\cos^2\theta+\left(1-2\varphi\right)^2}+\frac{\left(2\varphi-1\right)\sqrt{4\left(1-\varphi^2\right)\cos^2\theta+5\varphi^2-4\varphi}}{4\left(1-\varphi^2\right)\cos^2\theta+\left(1-2\varphi\right)^2}, \quad (6)$$

where θ is the Lode angle, and φ is the ratio between the tensile meridian and the compressive meridian. The failure surface becomes a tensile meridian when θ=0, and a compressive meridian when θ=π/3. The corresponding shapes of the deviatoric plane are shown in Fig. 2, and θ is defined as

$$\cos(3\theta)=\frac{3\sqrt{3}}{2}\frac{|\boldsymbol{s}_{ij}|}{J_2^{3/2}}, \quad (7)$$

where $\boldsymbol{s}_{ij}$ is the deviatoric stress tensor, and J_2 is the second invariant of stress deviation. The ratio between the tensile meridian and the compressive meridian φ is determined by the following equation:

$$\varphi(P)=\begin{cases}0.5, & P\le 0,\\ 0.5+1.5\dfrac{T}{f_c}, & P=f_c/3,\\ \dfrac{1.15}{1-B\left(\frac{1}{3}\right)^N+B\left(\frac{2.3}{3}\right)^N}, & P=\dfrac{2.3}{3},\\ 0.753, & P=3f_c,\\ 1, & P\ge 8.45f_c.\end{cases} \quad (8)$$

To ease the numerical computations, $\varphi(P)$ was interpolated linearly in the discontinuous regions of Eq. (8).

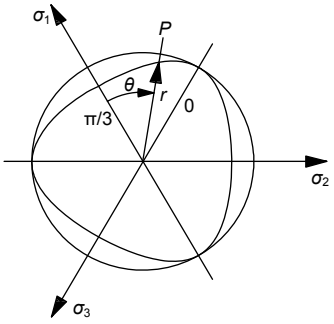

Fig. 2 Yield surface shape in the deviatoric plane

σ_1, σ_2, and σ_3 are the first, second, and third principal stresses, respectively; r is the ratio between the current meridian and the compressive meridian

2.3 Accumulation of damage

The stress state was divided into hydrostatic pressure and deviatoric stress components. Therefore, when the material transitions into the plastic state, the deviatoric stress will decrease as the plastic strain increases. Moreover, the hydrostatic pressure will increase with the accumulation of plastic volumetric strain. However, given that concrete is porous by nature, the voids inside the concrete will collapse at increasing hydrostatic pressure. Therefore, the degradation of material performance due to volumetric strain should be accounted for in a dynamic constitutive model. For example, Gebbeken and Ruppert (2000) obtained excellent results when they incorporated the following damage accumulation equation in their numerical simulations of concrete targets exposed to explosive contact charges.

$$\Delta\lambda_v=\alpha_m\left(\frac{\mu-\mu_{crush}}{\mu_{lock}-\mu_{crush}}\right)^{\alpha_m-1}, \quad (9)$$

where $\Delta\lambda_v$ is the volumetric compression damage factor increment, μ is the volumetric strain, and α_m is the parameter that controls the mode of damage softening, with $\alpha_m>1$ denoting brittle softening, $\alpha_m<1$ ductile softening, and $\alpha_m=1$ linear softening. Hartmann et al. (2010) suggested an α_m value of 1.5. Also, μ_{crush} is the volumetric strain caused by compaction pressure, while μ_{lock} is the ultimate (compaction) volumetric strain of the concrete.

In this study, the damage accumulation factor is described using the plastic strain increment and plastic volumetric strain increment:

$$\lambda=\sum\Delta\lambda=\begin{cases}\sum\left(\Delta\varepsilon_p/\varepsilon_p^f+\Delta\lambda_v\right), & P>0,\\ \sum\Delta\varepsilon_p, & P\le 0.\end{cases} \tag{10}$$

where λ is the damage accumulation factor, $\Delta\varepsilon_p$ is the plastic strain increment, and ε_p^f is the amount of equivalent plastic strain before fracture.

Note that the deviatoric stress and cumulative plastic strain would approach zero when the stress paths approach triaxial tension paths, which will cause D_t also to approach zero. This is clearly inconsistent with reality. To solve this problem, Malvar et al. (1997) included a volumetric damage term in their concrete material model that was dependent on volumetric strain. We adopted a similar approach in this study. Accordingly, the expression of this volumetric term is as follows:

$$\Delta\lambda=c\times f_d\times\Delta\varepsilon_v,\quad P\le 0, \tag{11}$$

where c is a constant, $\Delta\varepsilon_v$ is the volumetric strain increment in each time step, and f_d is the factor that constrains the stress paths in the presence of triaxial tension, whose expression is

$$f_d=\begin{cases}1-\dfrac{\left|\sqrt{3J_2}/P\right|}{0.1}, & 0\le\left|\sqrt{3J_2}/P\right|<0.1,\\ 0, & \left|\sqrt{3J_2}/P\right|\ge 0.1.\end{cases} \tag{12}$$

The corrected nonlinear softening curve proposed by Reinhardt et al. (1986) was used as the tensile damage accumulation model. Fig. 3 shows that the matrix of the UHTCC will start to crack when the tensile load reaches the limit tensile strength of the material, T. However, the PVA fibers in the UHTCC, which hinder crack formation in the matrix, prevent the immediate degradation of the strength of the UHTCC. A large number of micro-cracks will form instead, until a primary tensile fracture forms. The strength of the material will decrease continuously as the plastic strain increases (Fig. 4). Therefore, we have defined the plastic strain values of $\varepsilon_{el}<\lambda\le\varepsilon_{multi}$ in the micro-crack formation and development stage (this is the fiber-dominated stage, in which the matrix of the UHTCC is primarily connected by PVA fibers). ε_{el} is the strain when the UHTCC matrix starts to crack, and ε_{multi} is the maximum tensile strain in the micro-crack formation and development stage. Eq. (13) describes the propagation of the micro-cracks when $\sum\Delta\lambda$ is greater than ε_{multi}, and $D_t^{multi}=1$.

$$D_t^{multi}=\sum\Delta\lambda/\varepsilon_{multi}. \tag{13}$$

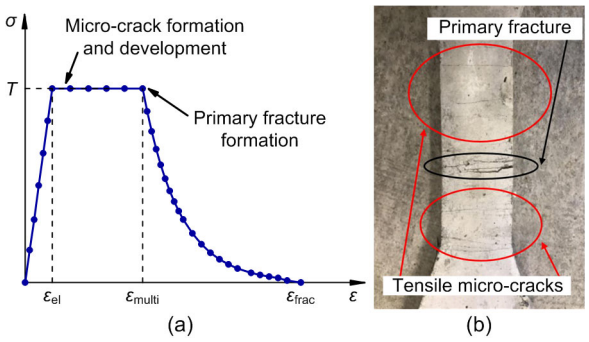

Fig. 3 UHTCC tensile stress–strain model (a) and experimental image (b) (ε_{frac} is the fracture strain)

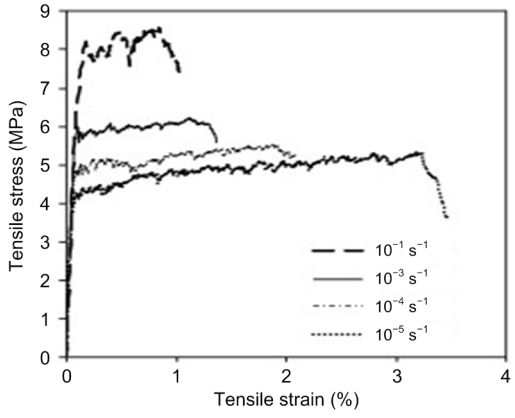

Fig. 4 UHTCC tensile stress–strain curves at different strain rates

The primary tension fracture occurs when plastic strains are developed such that $\varepsilon_{\text{multi}}<\lambda\leq\varepsilon_{\text{frac}}$. The following damage equation describes the tensile characteristics of UHTCC.

$$D_{\text{t}}=\begin{cases}0, & \lambda\leq\varepsilon_{\text{multi}},\\ \left[1+\left(c_1\dfrac{\lambda-\varepsilon_{\text{multi}}}{\varepsilon_{\text{frac}}-\varepsilon_{\text{multi}}}\right)^3\right]\mathrm{e}^{-c_2\frac{\lambda-\varepsilon_{\text{multi}}}{\varepsilon_{\text{frac}}-\varepsilon_{\text{multi}}}} & \\ \quad-\dfrac{\lambda-\varepsilon_{\text{multi}}}{\varepsilon_{\text{frac}}-\varepsilon_{\text{multi}}}\left(1+c_1^3\right)\mathrm{e}^{-c_2}, & \varepsilon_{\text{multi}}<\lambda\leq\varepsilon_{\text{frac}},\\ 1, & \lambda>\varepsilon_{\text{frac}},\end{cases} \tag{14}$$

where the constants c_1 and c_2 are equal to 3 and 6.93, respectively.

Based on experimental studies on the tensile strain hardening rate of ECC panels, Yang and Li (2014) demonstrated that increases in the tensile strain rate lead to increases in the tensile strength of ECC panels, and a continuous decrease in $\varepsilon_{\text{multi}}$ (Fig. 4). We obtained the relationship between $\varepsilon_{\text{multi}}$ and the logarithmic strain rate $(\lg\dot{\varepsilon}+5)$ by fitting the experimental data of Yang and Li (2014) (Fig. 5). In this way, the tensile characteristics of the UHTCC can be accurately described at different strain rates based on the damage function; the relationship between $\varepsilon_{\text{multi}}$ and the strain rate is expressed as

$$\varepsilon_{\text{multi}}=\frac{0.032\left[1-0.676\left(\lg\dot{\varepsilon}+5\right)\right]}{1+0.676\left(\lg\dot{\varepsilon}+5\right)}. \tag{15}$$

The typical tensile stress–strain curve of UHTCCs subjected to quasi-static loading can be simplified to the curve shown in Fig. 6. Throughout the fracturing of a UHTCC, it is assumed that the fracture energy of the UHTCC is constant and satisfies the following equation (Li and Xu, 2011):

$$\begin{aligned}\int_{\varepsilon_{\text{el}}}^{\varepsilon_{\text{frac}}}\sigma\mathrm{d}\varepsilon=\frac{G_{\text{f}}}{h_{\text{c}}}&\approx\int_0^{\varepsilon_{\text{frac}}}T(1-D_{\text{t}})\mathrm{d}\varepsilon_{\text{p}}\\&=\varepsilon_{\text{multi}}T+0.195T\varepsilon_{\text{frac}},\end{aligned} \tag{16}$$

where G_{f} is the static fracture energy, and h_{c} is the width of the fracture opening. In this work, fractures are defined to open within a single element. Therefore, h_{c} is the size of an element, which can be obtained by taking the cubic root of the volume of an element in the 3D model (Tu and Lu, 2009).

Based on Eq. (10), the fracture strain of a UHTCC under static tension is

$$\varepsilon_{\text{frac}}=\frac{5.136G_{\text{f}}}{h_{\text{c}}T}-\frac{\varepsilon_{\text{multi}}}{0.195}. \tag{17}$$

The compression damage is defined as

$$D_{\text{c}}=\alpha_{\text{c}}\lambda^{\alpha_{\text{d}}}/(1+\lambda+\alpha_{\text{c}}\lambda^{\alpha_{\text{d}}}), \tag{18}$$

where α_{c} and α_{d} are parameters that control compression softening.

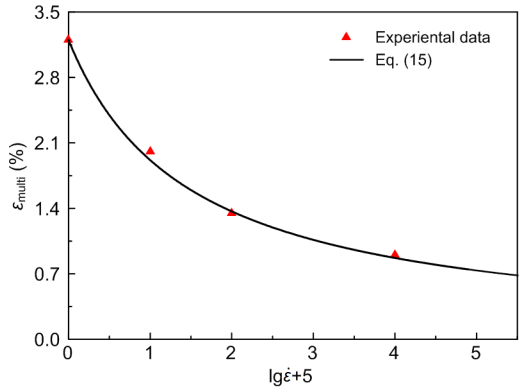

Fig. 5 Relationship between $\varepsilon_{\text{multi}}$ and logarithmic strain rate $(\lg\dot{\varepsilon}+5)$

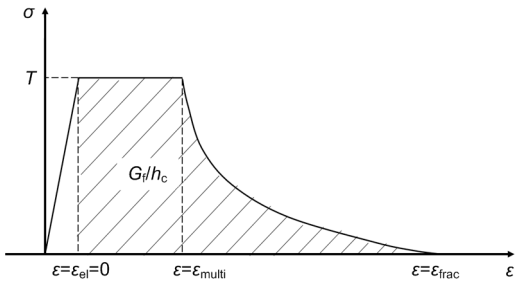

Fig. 6 Typical stress–strain curve of a UHTCC for uniaxial tension

Zhao (2018) normalized the compressive stress–strain curves of a UHTCC at strain rates in the range of 103.7–246.9 s^{-1}, according to its peak stress (σ/σ_{p}) and peak strain ($\varepsilon/\varepsilon_{\text{p}}$). In this way, Zhao (2018) fitted the dynamic compressive stress–strain curves of the UHTCC at different strain rates, based on the

results of static compression tests and experimental data describing the rate effect on the UHTCC's dynamic peak stress and dynamic peak strain. In this study, the abovementioned normalized compression stress–softening curve was used to determine the compressive damage function, D_c (Fig. 7). The parameters of this curve were taken from the aforementioned normalized stress–strain curves, and were amended according to the results of the dynamic mechanical tests.

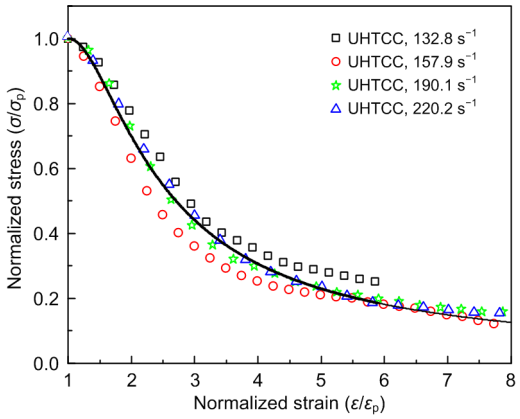

Fig. 7 Normalized compression stress–softening curves of a UHTCC at different strain rates

2.4 Strain rate effect

A significant increase in the strength of concrete-like materials under dynamic loads with high strain rates is always found (Lin, 2018). UHTCC is a cementitious composite material with a significant strain rate effect, like concrete (Li et al., 2016a). Therefore, to obtain accurate numerical prediction results, it is very important to take into account the strain rate effect in the UHTCC constitutive model.

Using the "radial enhancement" approach, the yield surface and compressive damage equations that account for the strain rate effect are defined as

$$\begin{aligned}\sigma_{\mathrm{eq}} &= \mathrm{DIF}\,\sigma_{\mathrm{eq}}\left(P/\mathrm{DIF}\right),\\ D_{\mathrm{c}} &= D_{\mathrm{c}}\left(P/\mathrm{DIF}\right)\big/\mathrm{DIF}.\end{aligned} \tag{19}$$

where DIF is the dynamic increased factor.

Considering the consistency between the experimental results and the hydrostatic pressure, we describe the rate dependence of DIF with the following formula:

$$\begin{aligned}\mathrm{DIF} &= \mathrm{DIF}(\dot{\varepsilon}, P^*)\\ &= \begin{cases}\mathrm{DIF_c}, & 3P^* \ge \mathrm{DIF_c},\\ \mathrm{DIF_c} - \dfrac{3P^* - \mathrm{DIF_c}}{\mathrm{DIF_c} + \mathrm{DIF_t}T^*}\left(\mathrm{DIF_t} - \mathrm{DIF_c}\right), & \\ & \mathrm{DIF_c} > 3P^* > -\mathrm{DIF_t}T^*,\\ \mathrm{DIF_t}, & -\mathrm{DIF_t}T^* > 3P^*,\end{cases}\end{aligned} \tag{20}$$

where $\mathrm{DIF_c}$ and $\mathrm{DIF_t}$ are DIFs defined for compression and tension, respectively.

Using a Split-Hopkinson pressure bar (SHPB) dynamic compression test, Zhao (2018) investigated the behavior of UHTCC at various strain rates. Based on data from a number of impact compression tests, Zhao (2018) proposed dynamic compression $\mathrm{DIF_c}$ equations for low-strength UHTCC materials, expressed as

$$\mathrm{DIF_c} = \begin{cases}1.0580 + 0.0097\lg\dot{\varepsilon}, & \dot{\varepsilon} \le 93.7\ \mathrm{s}^{-1},\\ -1.6323 + 1.3742\lg\dot{\varepsilon}, & \dot{\varepsilon} > 93.7\ \mathrm{s}^{-1}.\end{cases} \tag{21}$$

Fig. 8 shows the comparison among $\mathrm{DIF_c}$ relations suggested by Conmite Euro-International (CEB) (Béton, 1993) and Zhao (2018), as well as test data, which indicates that the models recommended by CEB significantly overestimate the test data. The formula proposed by Zhao (2018) shows better agreement with the experimental data.

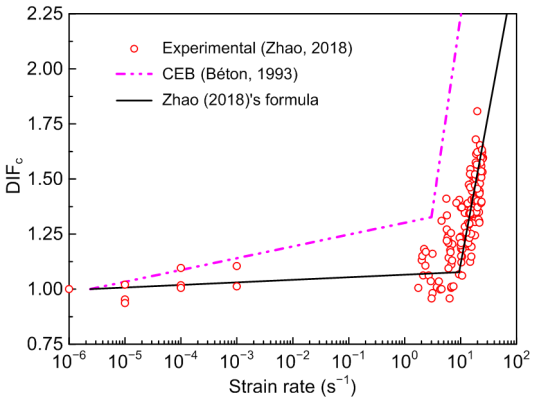

Fig. 8 $\mathrm{DIF_c}$ for compressive strength of UHTCCs

The dynamic tensile behavior of UHTCC is also sensitive to the loading rate, and in this case, many studies have been devoted to this effect. Li and Xu (2016) conducted a direct tensile test of UHTCC with

a strain rate in the range of 10^{-6}–0.1 s^{-1}. The results showed that the dynamic tensile strength of UHTCC continuously increased with the strain rates, while the trend of failure tensile strain against strain rates did not. However, using a strain rate in the range of 10^{-5}–0.1 s^{-1}, Yang and Li (2014) found that the tensile strength of UHTCC increased by 70% at the highest strain rate and the dynamic tensile strain decreased with the strain rate. Ranade et al. (2015) found that with increasing strain rate, the average tensile strain of high-strength and high-toughness UHTCC decreased from 4.2% to 2.7%. Zhao (2018) investigated a dynamic split test on UHTCC with a strain rate in the range of 1–10.4 s^{-1}, and obtained a large amount of dynamic tensile test data (Fig. 9). Combining the test data of Li and Xu (2016), Ranade et al. (2015), and Mechtcherine et al. (2011), a UHTCC dynamic tensile DIF_t model from static to dynamic was established, as shown in the following formula:

$$\mathrm{DIF_t}=\begin{cases}1.1995+0.3523\lg\dot{\varepsilon}, & \dot{\varepsilon}\le 3.67\ \mathrm{s^{-1}},\\ 0.5572+1.1720\lg\dot{\varepsilon}, & \dot{\varepsilon}>3.67\ \mathrm{s^{-1}}.\end{cases} \tag{22}$$

Fig. 9 shows a comparison between the experimental data and the values of DIF_t predicted from Eq. (22) (Zhao, 2018) and those obtained by CEB model code (Béton, 1993) for UHTCC. We conclude that Eq. (22) (Zhao, 2018) is in good agreement with the experimental data.

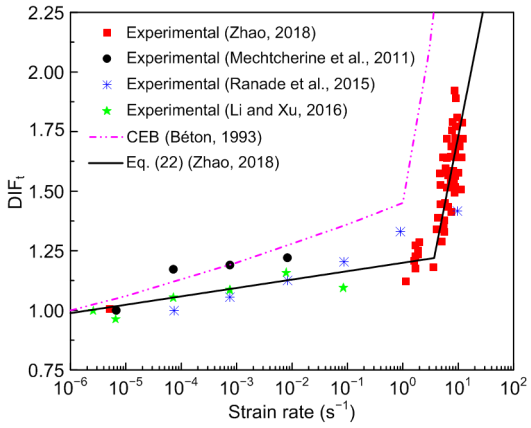

Fig. 9 DIF_t for tensile strength of UHTCCs

Using the DIF formulas of Zhao (2018), as no cutoff value is defined, the predicted strength enhancement would reach 10–100 times, which is unrealistic. Xu and Wen (2013) introduced cutoffs of 2.94 for DIF_c, and 10.0 for DIF_t in their model, which can avoid the overestimation of DIF at high strain rates, and were used in the present study.

2.5 Equation of state

The relationship between hydrostatic pressure and volumetric strain in our new model is controlled by the piecewise equation of state (Fig. 10). The first stage is the elastic stage, which starts from a negative pressure equal to $-T(1-D_t)$ and extends up to the elastic limit P_{crush}, expressed as

$$P=K\mu,\quad -T(1-D_t)\le P\le P_{crush}, \tag{23}$$

where K is the bulk modulus of the material.

Stage two is the plastic stage, in which the voids inside the UHTCC are gradually compacted. This manifests as compression damage due to the accumulation of plastic volumetric strain. The loading process will proceed along the path shown in Fig. 6. A new load will first proceed along the unloading path up to the unloading point, and will then continue along the loading path. The loading and unloading equations are

$$\begin{cases}P=\dfrac{(\mu-\mu_{crush})(P_{lock}-P_{crush})}{\mu_{plock}-\mu_{crush}}+P_{crush}, & \text{loading},\\ P=P_0-\left[(1-F)K+FK_1\right](\mu_0-\mu), & \text{unloading},\end{cases} \tag{24}$$

where μ_{plock} is the volumetric strain corresponding to the compaction stress P_{lock}. P_0 is the stress that corresponds to the volumetric strain prior to unloading, μ_0, and F=(μ_0−μ_{crush})/(μ_{plock}−μ_{crush}) is the proportionality coefficient. K_1 is a pressure constant.

During the third stage, the voids inside the UHTCC have been fully compacted. The UHTCC is assumed to exhibit nonlinear elastic compression behavior in this stage, and the loading process will follow the path shown in Fig. 10, that is

$$\begin{cases}P=K_1\bar{\mu}+K_2\bar{\mu}^2+K_3\bar{\mu}^3, & \text{loading},\\ P=K_1\bar{\mu}, & \text{unloading},\end{cases} \tag{25}$$

where $\bar{\mu}$ =(μ−μ_{lock})/(1+μ_{lock}) is the corrected volumetric strain, and K_2 and K_3 are pressure constants.

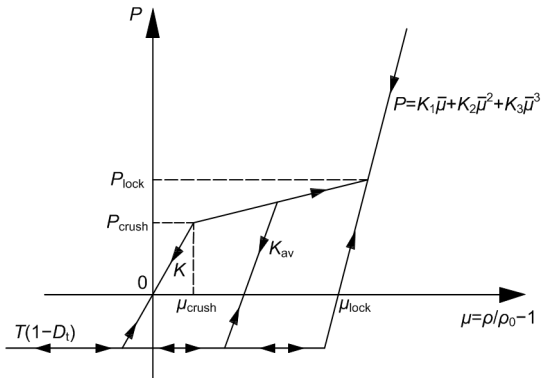

Fig. 10 Equation of state

K_{av} is the unloading modulus of the material; ρ/ρ_0 is the ratio between the current and the initial densities

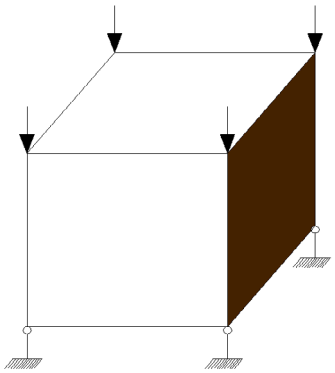

Fig. 11 Single element model

Table 1 Parameters of the new constitutive model

Parameter	Value	Parameter	Value
ρ (kg/m^3)	2124	P_{crush} (MPa)	11.13
G (MPa)	7150	P_{lock} (MPa)	1000
K (MPa)	9566	D_1	0.04
B	1.80	D_2	1
N	0.8	c_1	3.0
c	0.33	c_2	6.93
f_c (MPa)	33.89	K_1 (MPa)	8.5×10^3
T (MPa)	3.86	K_2 (MPa)	-1.71×10^5
G_f (N/m)	5371	K_3 (MPa)	2.08×10^5
ε_{fmin}	11	α_m	1.5
μ_{crush}	1.1×10^{-3}	α_c	6.694
μ_{lock}	0.1	α_d	1.84

G is the shear modulus of the material

Table 2 Parameters of the HJC constitutive model

Parameter	Value	Parameter	Value
ρ (kg/m^3)	2124	P_{crush} (MPa)	11.13
G (MPa)	7150	P_{lock} (MPa)	1000
A	0.295	μ_{crush}	1.1×10^{-3}
B	1.83	μ_{lock}	0.1
C	0.007	D_1	0.04
N	0.63	D_2	1
f_c (MPa)	33.89	K_1 (MPa)	8.5×10^3
T (MPa)	3.86	K_2 (MPa)	-1.71×10^5
ε_{fmin}	0.01	K_3 (MPa)	2.08×10^5
S_{max}	11	epso	1.0

epso is the quasi-static threshold strain rate

3 Model validation

LS-DYNA is a powerful explicit dynamic finite element analysis software package, which has a large variety of built-in material models, as well as an interface for users to define their own material models. The model proposed in this study was embedded in LS-DYNA to create a new solver. To validate the correctness of the UHTCC elastoplastic damage constitutive model established in this study and determine partial parameters related to tensile and compression damage, the stress–strain curves of UHTCC materials under quasi-static and dynamic loading conditions were predicted by a single element (Fig. 11). The curves were compared with experimental data and the predicted results from the HJC and K&C models. The parameters of the 34.3-MPa UHTCC model that were used to test our constitutive model are listed in Table 1. The density, compressive strength, tensile strength, elastic modulus, and Poisson's ratio of UHTCC were obtained from the experiment, whereas the B and N values were fitted to the data from triaxial compression tests (Fig. 2). The reference values provided by Xu et al. (2019) were used for the remaining parameters. The HJC model parameters for a 34.3-MPa UHTCC are listed in Table 2. The K&C model parameters were generated automatically using compressive strength and density.

3.1 Static test results

To calibrate the proposed model in accordance with experimental results, several loading conditions were selected as follows: uniaxial compression, uniaxial tension, biaxial compression, and triaxial compression with confining pressures of 5, 10, or 15 MPa. However, the above loading tests were carried out under quasi-static loading conditions. Note that an

explicit dynamic algorithm was adopted to simulate the above experimental tests in this study. This made it impossible to carry out the loading simulation for a long time because the amount of calculation would have increased exponentially. Therefore, if the strain rate effect in the constitutive model is removed from the simulation in the above experiments, the numerical calculation result becomes independent of the loading rate, and the quasi-static loading experiment can be simulated at a higher loading rate.

3.1.1 Uniaxial testing

The uniaxial tensile stress–strain curves that were simulated by the HJC model, K&C model, and our proposed model for the 34.3-MPa UHTCC are compared to the experimental curve in Fig. 12a. The HJC model significantly overestimated the uniaxial tensile strength of the UHTCC. This is because the HJC model does not account for the effects of the Lode angle in UHTCCs, nor does it have a specific definition for tensile damage. Therefore, the HJC model cannot accurately describe the uniaxial tensile strength and tension softening behaviors of the UHTCC. Although the K&C model can predict the uniaxial tensile strength and tensile softening behavior of UHTCC, it cannot describe the limited tensile ductility of UHTCC. By contrast, the proposed model can accurately describe the tensile strain hardening and tension softening behaviors of the UHTCC.

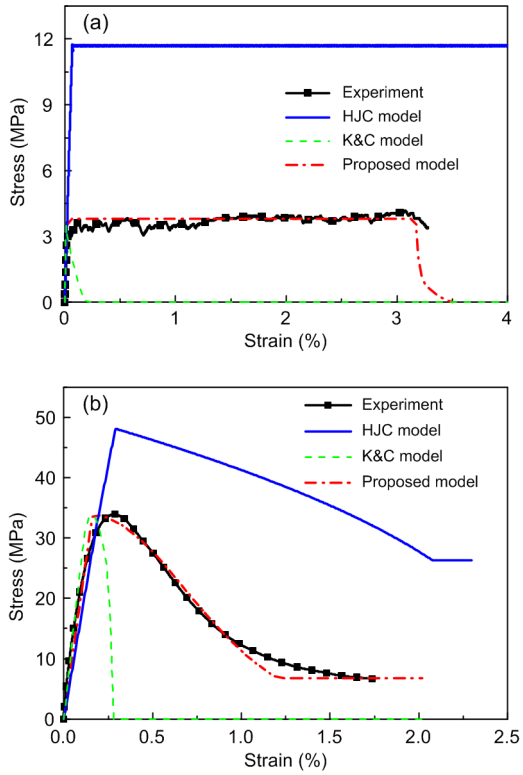

Fig. 12 Comparisons of experimental data of uniaxial tensile (a) and compressive (b) stress–strain curves of UHTCC with predictions from the three models

Fig. 12b illustrates the results of simulated uniaxial compression tests based on three models: HJC, K&C, and our proposed models. Compared to the experimental results, the HJC model did not reproduce an accurate uniaxial compressive strength, due to the overestimation of the failure surface at $P=f_c/3$ (Fig. 2) and the plastic softening gradient. The K&C model clearly overestimated the softening behavior of UHTCC. Comparatively, the results predicted from our UHTCC model were in good agreement with the experimental data.

3.1.2 Biaxial testing

Pan et al. (2016) used a true triaxial tester with hydraulic servos to perform biaxial compression tests on 34.3-MPa ECC materials, with a pressure ratio of 1. The biaxial compression stress–strain curve was simulated using the HJC model, K&C model, and our proposed model. The simulated and experimental results are shown in Fig. 13. The peak strength and peak strain predicted by the HJC model for the ECC material were significantly higher than the corresponding experimental values. Although the K&C model could predict the UHTCC biaxial compression strength better, it could not predict the UHTCC biaxial compression peak strain, and the strain-softening gradient was greater than that from the experimental results. In contrast, the biaxial compression curves simulated by the proposed model was consistent with the experimental curves.

3.1.3 Triaxial testing

Wen (2015) performed conventional triaxial compression tests on PVA–UHTCC materials with a water-to-binder ratio of 0.32. Fig. 14 shows the triaxial compression stress–strain curves predicted by the HJC, K&C, and our proposed models for an ECC at different confining pressures. The HJC and K&C models overestimated the peak stress of the UHTCC under corresponding confining pressures, and the strain softening gradient predicted by the K&C model

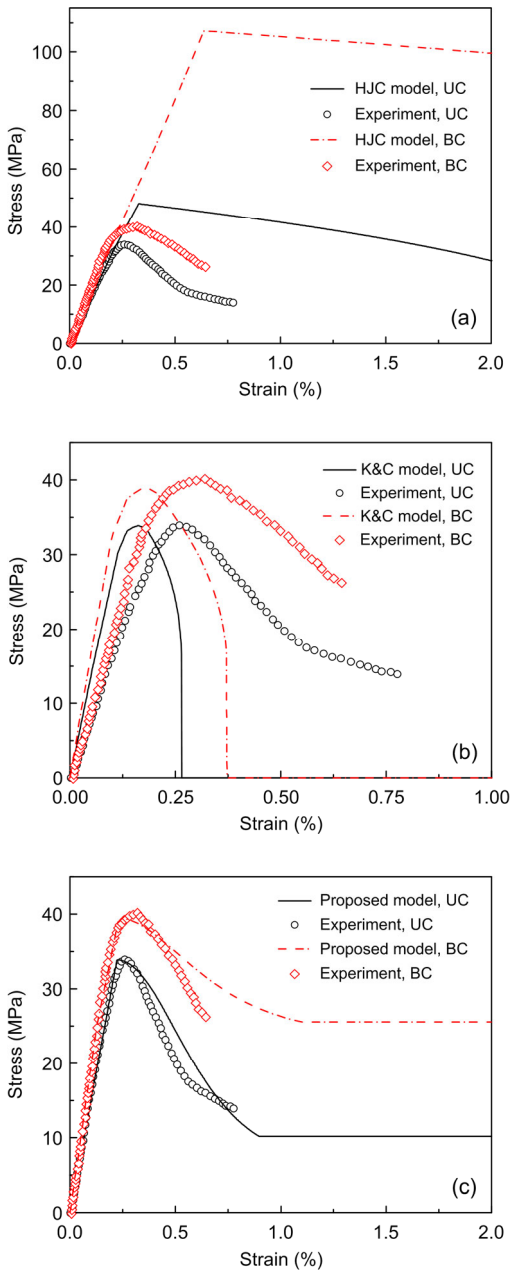

Fig. 13 Comparisons of the experimental stress–strain relationships of UHTCC in uniaxial compression (UC) and biaxial compression (BC) with predictions from: (a) HJC model; (b) K&C model; (c) our proposed model

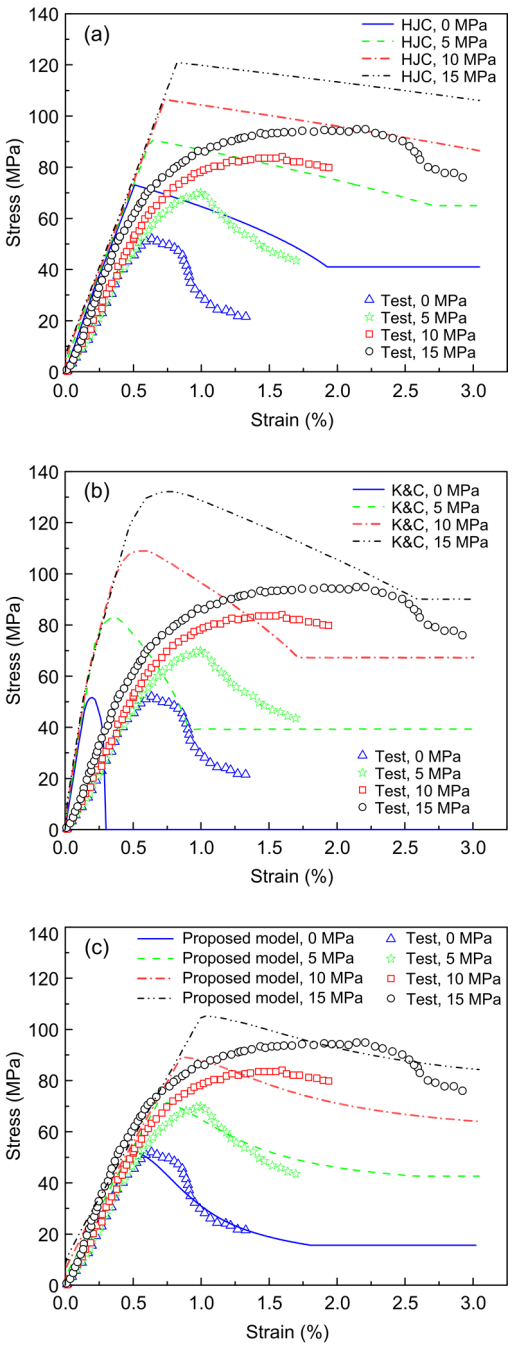

Fig. 14 Comparisons of the experimental stress–strain curves of UHTCC in triaxial compression with predictions from: (a) HJC model; (b) K&C model; (c) our proposed model

was larger than that from the experiment results. The peak stress and strain softening behaviors predicted by our model were closed to the experimental results.

3.2 Dynamic test results

The mechanical behaviors of UHTCCs numerically predicted by the HJC, K&C, and our proposed models at high strain rates were compared in the form of uniaxial compression and tensile stress–strain curves under different strain rates. The biaxial and triaxial tensile stress–strain relationships at the strain rate of 10 s^{-1} are also presented.

3.2.1 Uniaxial compression strain rate test

Fig. 15 shows the uniaxial compression stress–strain diagrams of the UHTCC predicted by the three models under the strain rates of 0.1, 1, 10, 100, and 300 s^{-1}, respectively. The uniaxial compressive strength predicted by the HJC model at a strain rate of 1 s^{-1} was 4% higher than that at a strain rate of 0.1 s^{-1}. However, the uniaxial compressive strength in the HJC model decreased by 1% at a strain rate of 10 s^{-1}, and by 20% at a strain rate of 100 s^{-1}, compared with the rate at 0.1 s^{-1}, which is inconsistent with the actual situation. The uniaxial compressive strengths predicted by the K&C model and the proposed model increased with increasing strain rate. The uniaxial compressive strength predicted by the K&C model was greater than that predicted by the UHTCC model proposed in this study. The compressive strength predicted by the K&C model increased more than 4 fold when the strain rate exceeded 100 s^{-1}, which contradicts Xu and Wen (2013)'s proposal that the increase in compressive strength of concrete materials should not exceed 3 fold due to the strain rate effect. The result predicted from our proposed model did not increase significantly when the strain rate was less than 100 s^{-1}, but when the strain rate exceeded 100 s^{-1}, the increase in compressive strength was more significant, which is consistent with Zhao (2018)'s UHTCC dynamic compression experiment results.

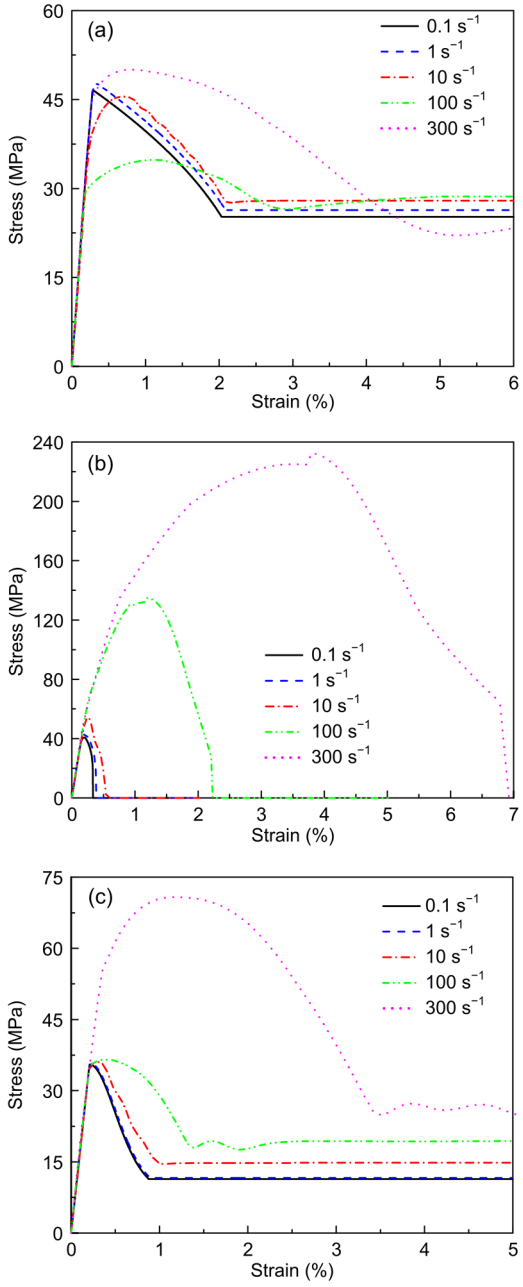

Fig. 15 Dynamic compressive stress–strain curves predicted under different strain rates by: (a) HJC model; (b) K&C model; (c) our proposed model

3.2.2 Uniaxial tensile strain rate test

Fig. 16 shows the dynamic tensile stress–strain curves predicted by the three material models at strain rates of 1, 10, and 100 s^{-1}. The tensile strength predicted by the HJC model was almost identical at strain rates of 1 and 10 s^{-1}, but when the strain rate was 100 s^{-1}, the plastic section of the stress–strain curve showed serious vibration, which was inconsistent with the experimental results. The tensile softening predicted by the K&C model decreased linearly. At the same time, the tensile strength, fracture strain, and fracture energy improved with increasing strain rate. However, the experimental data show that the fracture strain of the concrete materials was constant, and the fracture energy grew with increasing strain rate (Schuler et al., 2006; Weerheijm and van Doormaal, 2007). The proposed model can better describe the tensile ductility of UHTCC materials, which will decrease with increasing strain rate. Tensile strength will increase with increasing strain rate, and the fracture strain is a fixed value.

3.2.3 Biaxial tensile test

The results of the biaxial tension tests simulated by the three models are shown in Fig. 17. The biaxial tensile ultimate strength and tensile softening were not predicted by the HJC model. Although the K&C

model reflected the softening behavior and rate effect of the biaxial tensile curve, it did not describe the tensile ductility characteristics of UHTCC. Compared with these two models, the model proposed in this study better described the limited tensile ductility, strain rate effect, and strain softening characteristics of UHTCC under the biaxial tensile condition.

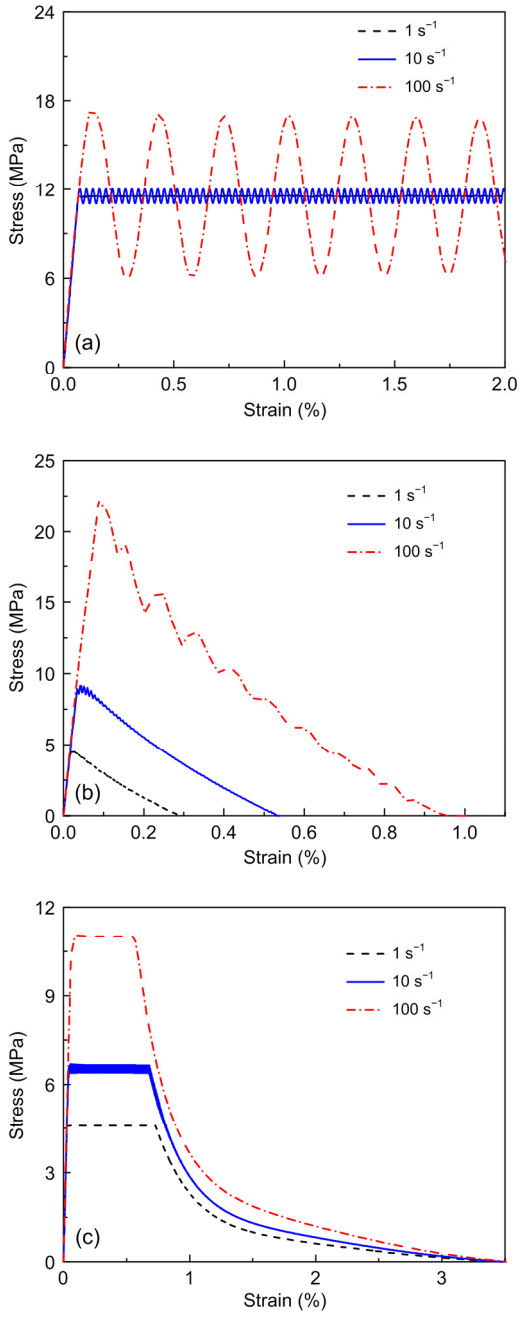

Fig. 16 Dynamic tension stress–strain curves predicted under different strain rates by: (a) HJC model; (b) K&C model; (c) our proposed model

3.2.4 Triaxial tensile test

As shown in Fig. 18, the HJC and K&C models were unable to simulate the strain softening of the triaxial tension curve and strain rate effect of triaxial tension, which is inconsistent with the concrete triaxial tension curve recommended by Weerheijm and van Doormaal (2007). However, the UHTCC constitutive model described not only the rate effect and strain softening of the triaxial tensile curve, but also the triaxial limited tensile ductility of UHTCC. The influence of the tensile volume damage parameter c on the stress–strain curve for triaxial tension is shown in Fig. 18. As c increased, the triaxial tensile ductility decreased and the strain softening gradient increased.

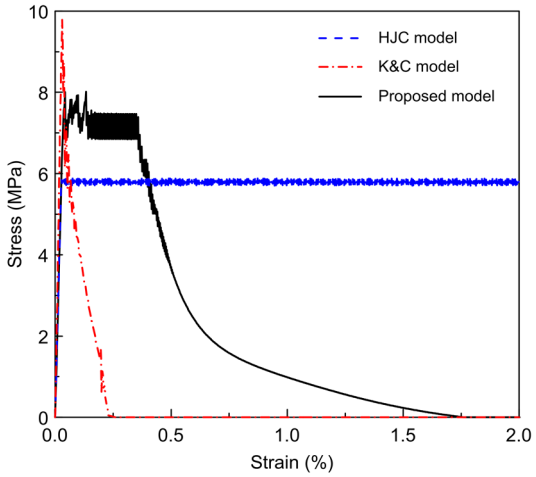

Fig. 17 Stress–strain curves of the biaxial tension test predicted by the three models

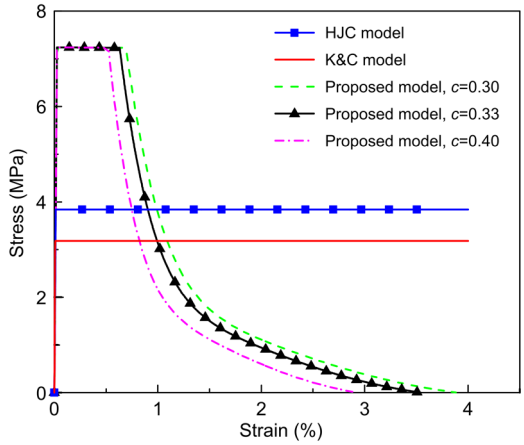

Fig. 18 Stress–strain curves of the triaxial extension test predicted by the three models

4 Numerical case study

4.1 UHTCC target subjected to blast by embedded explosive

To validate the accuracy of our proposed model, blast resistance tests on UHTCC targets were numerically simulated in LS-DYNA, with explosive charges buried at a certain depth. The results of this simulation were then compared to pre-existing experimental data.

4.1.1 Experiment overview

The UHTCC target was a cylinder with a diameter of 400 mm and a height of 240 mm. A cylindrical hole with a diameter of 33 mm was left at the center of the target. A cylindrical explosive charge with a diameter of 33 mm and a height of 50 mm was used, and the distance between the center of the explosive charge and the surface of the UHTCC target was 35 mm (Fig. 19). An amount of 50 g of emulsion explosive was used in this experiment, and an electric detonator was used to detonate the explosive charge.

Fig. 19 UHTCC target for the blast test

4.1.2 Finite element model

A numerical simulation was performed, in which 50 g of emulsion explosive was buried 60 mm inside the aforementioned UHTCC target. To reduce computational time and increase computational efficiency, we constructed only a 1/4 model (which should yield the same results as a full model based on symmetry) (Fig. 20). An m-s-kg system of units was used in this simulation. Arbitrary Lagrangian Eulerian (ALE) multi-material elements were used to model the explosive and air. The air domain covered the entire space in which the target was located, and a non-reflective boundary was defined at the outer surface of the air domain. The target was modeled using Lagrangian elements, and a fluid–solid coupling algorithm was used to account for the actions of air and the explosive charge on the target. The dimensions of the air and explosive charge elements were 5 mm×5 mm×5 mm, and the dimensions of the concrete elements were 3 mm×3 mm×3 mm. The finite element model contained a total of 2 141 904 elements.

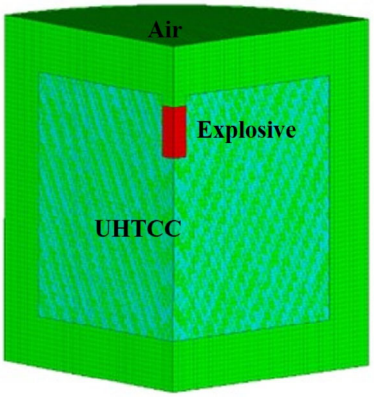

Fig. 20 Finite element model

4.1.3 Material models

A simplified model of air was used, in which air was treated as a non-viscous ideal gas with a linear polynomial equation of state whose expression is

$$P_{\mathrm{a}} = C_0 + C_1\mu + C_2\mu^2 + C_3\mu^3 + (C_4 + C_5\mu + C_6\mu^2)E_0, \tag{26}$$

where P_{a} is the air pressure. $\mu=V_0/V-1$, where V_0 is the initial relative volume, and V is the relative volume. E_0 is the initial internal energy density, and C_0–C_6 are the coefficients of the polynomial equation. The parameter values of the model are shown in Table 3 (LSTC, 2012).

The explosion of the charges was simulated with the use of a built-in explosion model (*MAT_HIGH_EXPLOSIVE_BURN) and state equation (*EOS_JWL) keywords in LS-DYNA. The Jones–Wilkins–Lee (JWL) state equation is usually expressed as

$$P_e = A_e\left(1-\frac{\varpi}{R_1V_e}\right)e^{-R_1V_e} + B_e\left(1-\frac{\varpi}{R_1V_e}e^{-R_2V_e} + \frac{\varpi E_e}{V_e}\right), \tag{27}$$

where P_e is the pressure generated by the detonation products, A_e, B_e, R_1, R_2, and ϖ are the state equation parameters, V_e is the relative volume of the detonation products, e is the specific internal energy, and E_e is the detonation energy per unit volume. The emulsion explosive used in this experiment had a density of 1100 kg/m^3 and a detonation velocity of 6700 m/s (Cheng, 2014). The values of the JWL state equation parameters are listed in Table 4.

Table 3 Parameters of the air material model

Parameter	Value	Parameter	Value
ρ (kg/m^3)	1.290	C_4	0.4
C_0	0	C_5	0.4
C_1	0	C_6	0
C_2	0	E_0 (MPa)	0.25
C_3	0	V_0	1.0

Table 4 Parameters of the JWL state equation of the explosive

Parameter	Value	Parameter	Value
A_e (GPa)	3.74	R_2	0.95
B_e (GPa)	3.25	ϖ	0.35
R_1	4.10	V_e	1.00

The constitutive model proposed in this study was used as the material model of the UHTCC. To predict crack propagation and target damage in the UHTCC target (which would be observed in the experiment), an element removal algorithm must be included in the numerical simulation of the blast resistance test. Based on the results of the blast test on the UHTCC target, we surmised that the material should have several (different) damage criteria depending on the forces acting on each part of the material. For example, the part below the explosive charge is subjected mainly to impact compression loads, whereas the parts around the side of the explosive charge will experience tensile loads. Therefore, we added erosion criteria to our material model to define material damage. The tension element removal algorithm uses the element removal criterion based on the fracture strain (ε_{frac}), whereas the compression element removal algorithm uses the maximum principle strain-based element removal criterion. The details are shown in Table 1.

4.1.4 Numerical simulation results

After the calculations, the d3plot files were post-processed in LS-PREPOST to obtain the compression damage contour maps that correspond to the detonation of the explosive charge buried inside the UHTCC target, as simulated by the HJC and proposed models. Fig. 21 shows that the simulations reproduced the size of the blast crater in the UHTCC target and the morphology of its internal damage. The size of the blast craters was measured using graphical measurement software. The blast crater was 240.5 mm in diameter and 69.8 mm deep in our proposed model, 211.6 mm in diameter and 86.3 mm deep in the HJC model, and 237 mm in diameter and 70.4 mm deep in the blast resistance test. The size of the blast crater in our proposed model was very similar to that of the experiment, with a total error of less than 5%. The HJC model underestimated the diameter of the blast crater, but overestimated its depth. This is because the HJC model overestimated the tensile and compressive strengths of UHTCC. Furthermore, this model did not account for the ability of the UHTCC matrix and fibers to absorb blast waves (Lai et al., 2016). The propagation of tensile micro-cracks and the formation of primary tension cracks due to the detonation of explosive charge inside the UHTCC target are illustrated in Figs. 22 and 23 (p.955). A significantly larger proportion of the target's surface was located in the tensile plastic zone rather than the compressive plastic zone. Within the tensile plastic zone, the area in the fiber-dominated stage (micro-crack propagation stage) was significantly larger than the area in the tensile softening stage. Furthermore, a large number of tensile micro-cracks and primary tension cracks had formed inside the target. These results are essentially identical to the experimental results.

4.2 UHTCC target subjected to projectile penetration

After the successful validation of the present model in terms of simulating the dynamic response of UHTCC under blast loading, further simulation was carried out to predict the damage resulting from projectile penetration, and simulation and test results were compared.

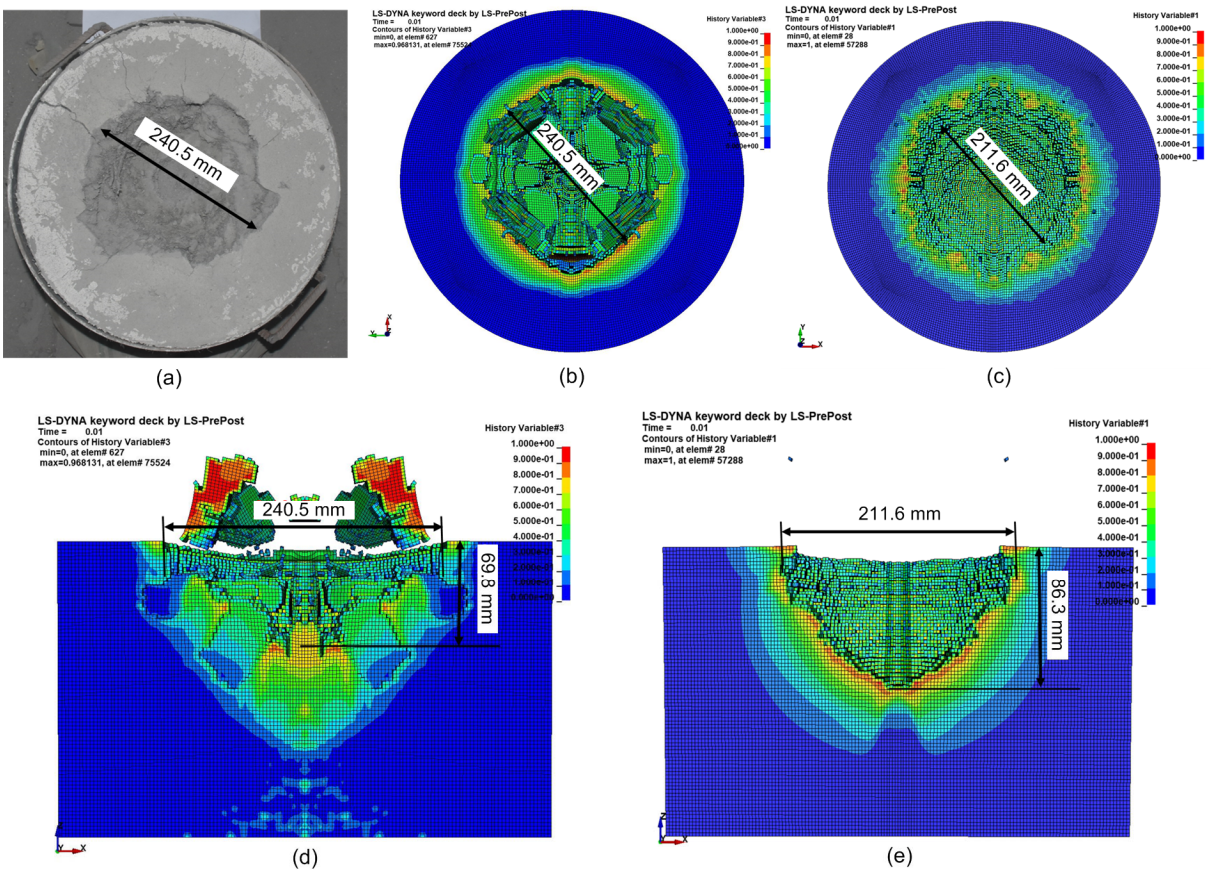

Fig. 21 Comparison of explosion experiment results (a) with compressive damage contours: (b) front surface (proposed model); (c) front surface (HJC model); (d) interior of the target (proposed model); (e) interior of the target (HJC model)

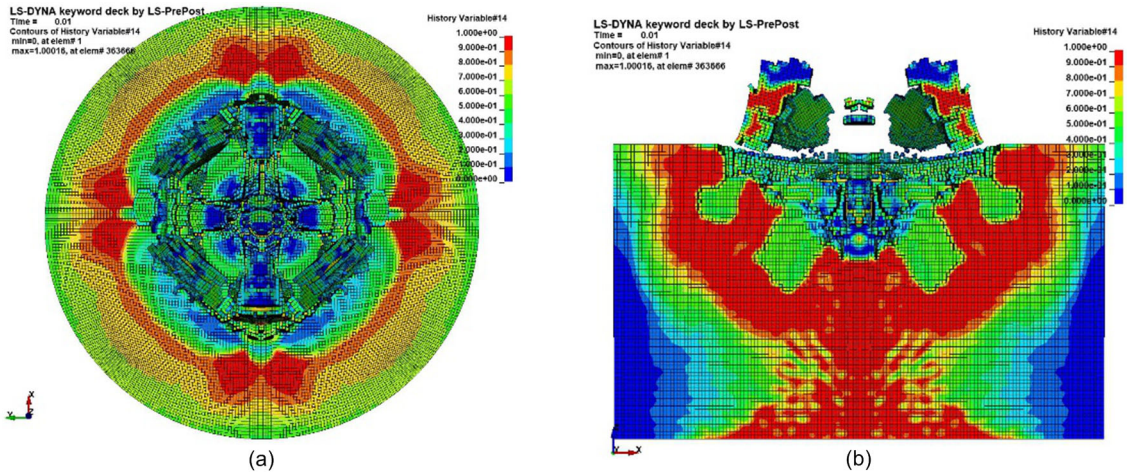

Fig. 22 Distribution of micro-cracks in the UHTCC target during explosion of 50-g emulsion explosive: (a) front surface; (b) interior of the target

4.2.1 Experiment overview

The size of the UHTCC target used in this test was Φ750 mm×600 mm, and the uniaxial compressive strength of the UHTCC was 33.9 MPa. The projectile had a diameter of 25 mm, a length of 152 mm, a warhead curvature CRH=3, a projectile density of 7850 kg/m^3, and a projectile mass of 340 g. The

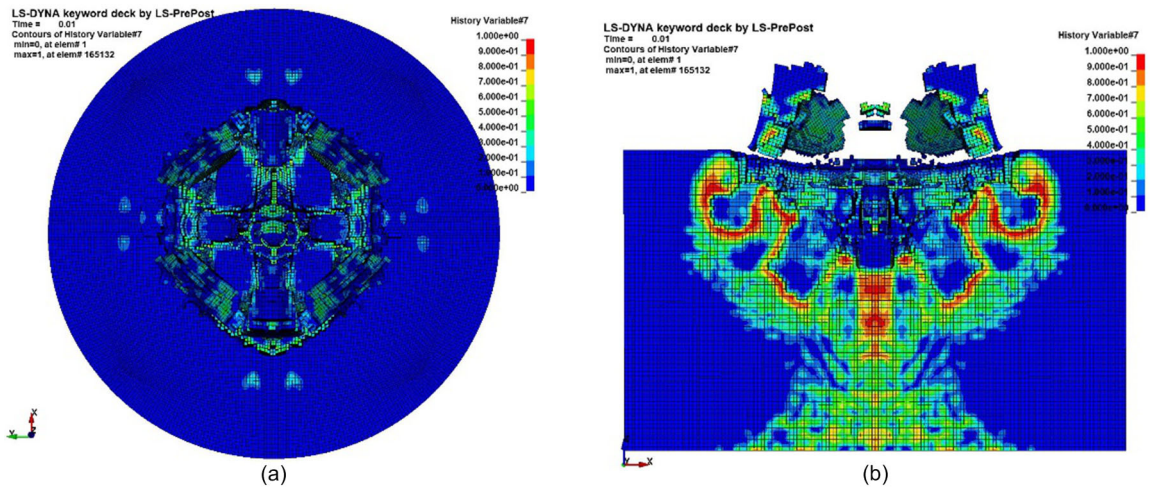

Fig. 23 UHTCC target tensile damage cloud following detonation of 50-g emulsion explosive: (a) front surface; (b) interior of the target

projectile penetrated the target at a speed of 570 m/s. The experimental device is shown in Fig. 24.

4.2.2 Finite element model

A finite element model was established according to the requirements of the test status and symmetry of the test situation. A 1/4 finite element model was built (Fig. 25). The projectile and UHTCC target both had SOLID164 solid elements. The contact between the projectile and the target was controlled by a CONTACT_ERODING_SURFACE_TO_SURFACE face-to-face erosion contact keyword. The model unit system was m-s-kg, and contained 3 698 000 nodes and 1 803 278 hexahedral elements. A rigid body model was used for the projectile, the specific parameters of which are shown in Table 5 (Wang et al., 2016). The model proposed in this study was adopted for the target body. The maximum principal strain was adopted as the deletion criterion of the UHTCC unit, and the threshold value was 0.2.

4.2.3 Numerical simulation results

Fig. 26 shows the experimental and simulation results of the projectile penetrating the UHTCC target at a speed of 570 m/s. The simulated crater size was 61 mm in our proposed model and 60 mm in the HJC model, and the experimental crater size was 67 mm. The simulated penetration depth was 372 mm in our proposed model and 381 mm in the HJC model, and the test penetration depth was 375 mm. The overall error did not exceed 5%. Thus, both the HJC model and our proposed model can accurately predict the depth of penetration of the projectile into the UHTCC

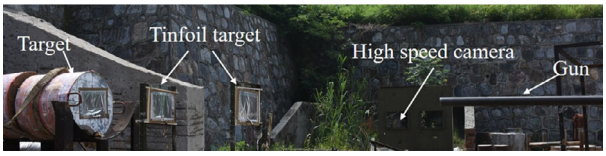

Fig. 24 Device used in penetration experiments

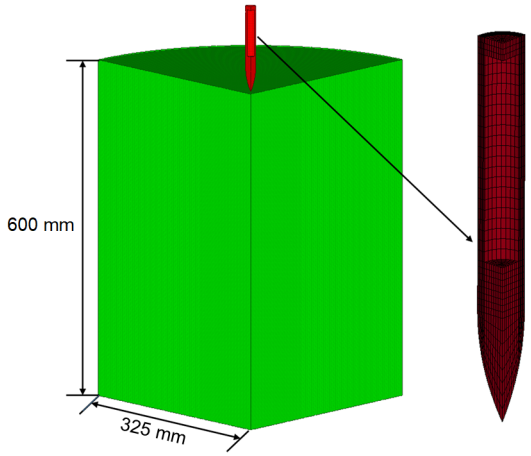

Fig. 25 Finite element model for penetration experiments

Table 5 Parameters of the projectile model

Parameter	Value
Density (kg/m^3)	7850
Elastic modulus (GPa)	210
Poisson's ratio	0.3

target and the diameter of the crater on the front face. Furthermore, Figs. 26b–26e show the compression damage caused by the projectile penetrating the target. The predicted damage was distributed mainly around the trajectory, and dense compression cracks were also generated near the crater on the face. However, the compressive damage cracks predicted by our model were more consistent with the experimental results than those predicted by the HJC model.

In addition, our model was able to predict the tensile micro-cracks and the main tensile cracks caused by the projectile penetrating the UHTCC target (Figs. 27 and 28), which intuitively shows the crack propagation of the test target's front surface.

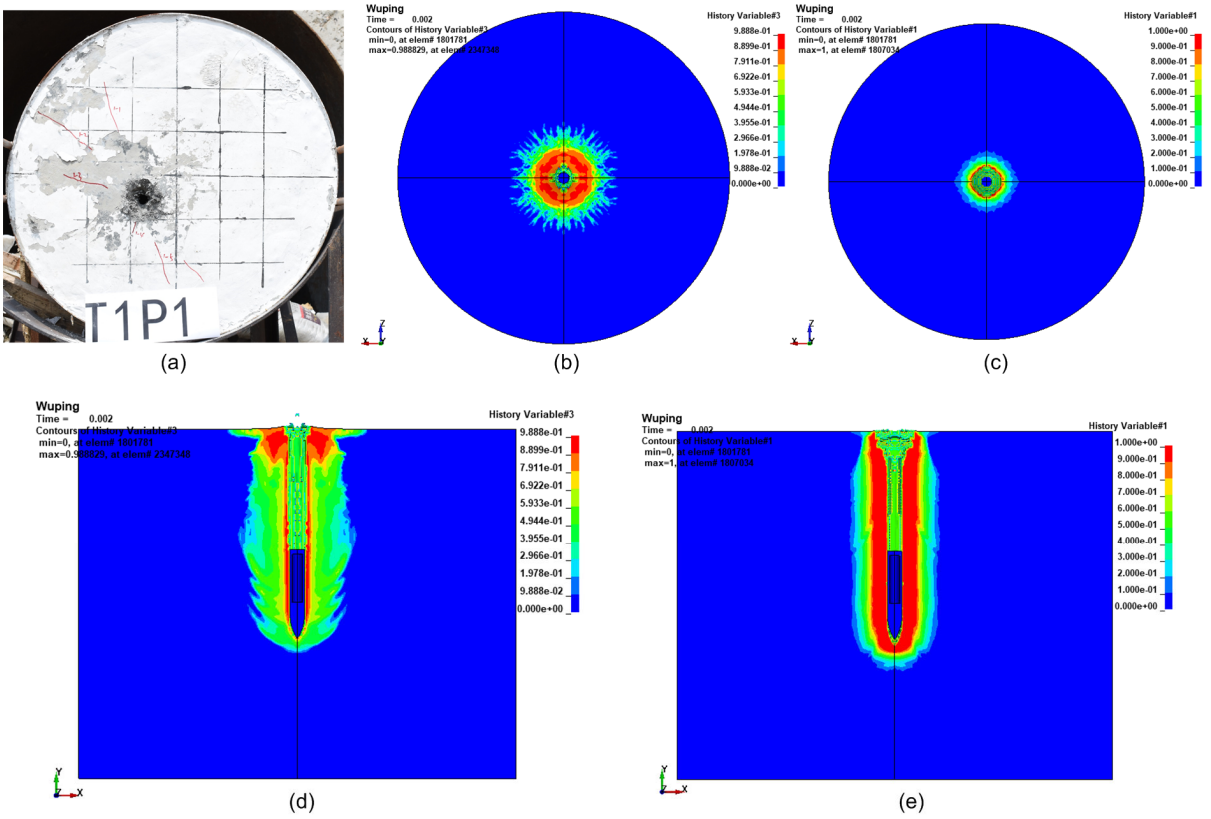

Fig. 26 Comparison of penetration experiment results (a) with compressive damage contours: (b) front surface (proposed model); (c) front surface (HJC model); (d) interior of the target (proposed model); (e) interior of the target (HJC model)

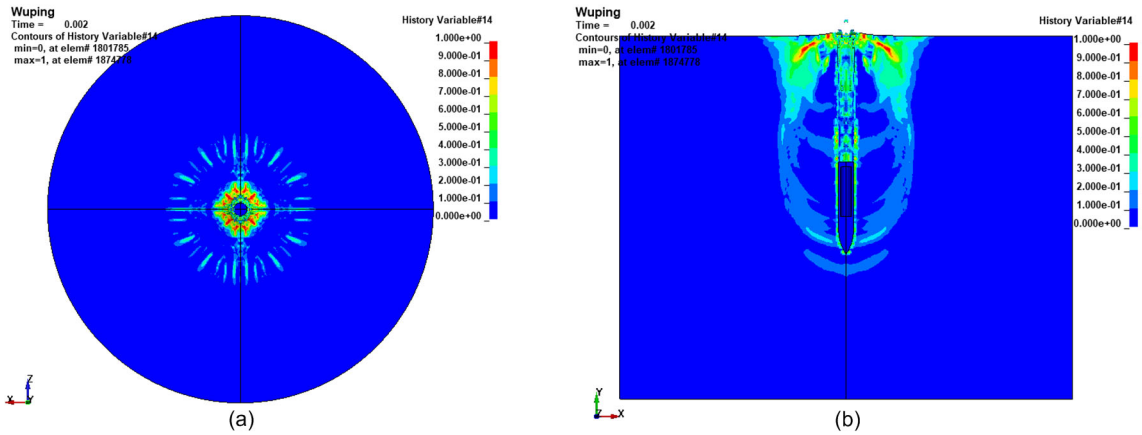

Fig. 27 Distribution of micro-cracks in the UHTCC target subjected to projectile penetration: (a) front surface; (b) interior of the target

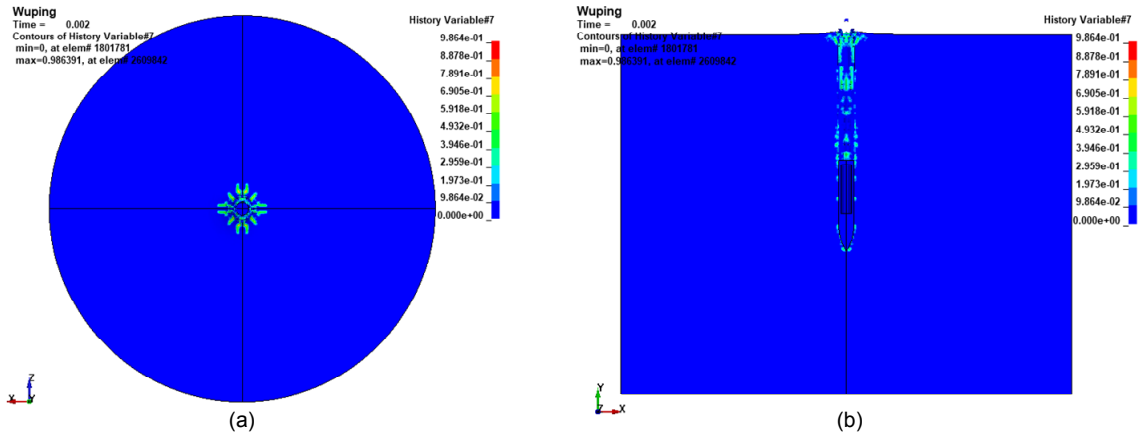

Fig. 28 Tensile damage to the UHTCC target subjected to projectile penetration: (a) front surface; (b) interior of the target

The tensile damage in the UHTCC target body was insignificant. This was due mainly to the bridging effect of the UHTCC matrix and the PVA fiber, giving the UHTCC excellent deformability, which absorbs the tensile stress waves formed by the projectile impacting the target body, greatly reducing the damage to the target body due to impact stretching (Wang et al., 2016).

5 Conclusions

By performing theoretical analyses on the elasto-plasticity of concrete materials and on the mechanical properties of UHTCC, a computational constitutive model suitable for UHTCC materials subjected to dynamic loadings was developed. The model was then implemented using an explicit dynamic finite element software package. The following conclusions were drawn from this study:

1. The dynamic constitutive model constructed for UHTCC materials accounted for pressure dependence, strain softening, strain rate effect, and porosity of these materials, and also reflected their ductile and tensile properties.

2. The proposed model was embedded in LS-DYNA and was used to simulate the stress–strain curves of a UHTCC material under uniaxial, biaxial, and triaxial tension and compression. The proposed model approximated the experimental data much more accurately than the HJC and K&C models, and could accurately reproduce the fundamental mechanical properties of UHTCC.

3. The UHTCC constitutive model was used to simulate the detonation of an explosive charge buried at a certain depth inside a UHTCC target. Based on comparisons with experimental data, our constitutive model was much more accurate (with errors of less than 5%) than the HJC model in predicting the size of the blast crater and the tension damage inside the UHTCC target.

4. The model proposed in this study can better predict the tensile and compressive damage failure of UHTCC materials under an impact load, and can show the distribution of tensile micro-cracks and compressive damage cracks in a UHTCC target.

Contributors

Shi-lang XU designed the research. Qing-hua LI and Ping WU processed the corresponding data. Ping WU wrote the first draft of the manuscript. Fei ZHOU, Xiao JIANG, and Bo-kun CHEN helped to organize the manuscript. Ping WU revised and edited the final version.

Conflict of interest

Shi-lang XU, Ping WU, Fei ZHOU, Xiao JIANG, Bo-kun CHEN, and Qing-hua LI declare that they have no conflict of interest.

References

Béton CEID, 1993. CEB-FIP Model Code 1990: Design Code. Thomas Telford, London, UK.

Cheng YF, 2014. Detonation Mechanism and Explosion Property of High-energy Emulsion Explosives Based on

Hydrogen Storage Material. PhD Thesis, University of Science and Technology of China, Hefei, China (in Chinese).

Gebbeken N, Ruppert M, 2000. A new material model for concrete in high-dynamic hydrocode simulations. *Archive of Applied Mechanics*, 70(7):463-478. https://doi.org/10.1007/s004190000079

Hartmann T, Pietzsch A, Gebbeken N, 2010. A hydrocode material model for concrete. *International Journal of Protective Structures*, 1(4):443-468. https://doi.org/10.1260/2041-4196.1.4.443

Holmquist TJ, Johnson GR, Cook WH, 1993. A computational constitutive model for concrete subjected to large strains, high strain rates, and high pressures. Proceedings of the 14th International Symposium on Ballistics, p.591-600.

Johnson GR, Cook WH, 1983. A constitutive model and data for metals subjected to large strains, high strain rates and high temperature. Proceedings of the 7th International Symposium on Ballistics, p.541-547.

Khan MZN, Hao YF, Hao H, et al., 2018. Mechanical properties of ambient cured high-strength plain and hybrid fiber reinforced geopolymer composites from triaxial compressive tests. *Construction and Building Materials*, 185: 338-353. https://doi.org/10.1016/j.conbuildmat.2018.07.092

Kong XZ, Fang Q, Wu H, et al., 2016. Numerical predictions of cratering and scabbing in concrete slabs subjected to projectile impact using a modified version of HJC material model. *International Journal of Impact Engineering*, 95:61-71. https://doi.org/10.1016/j.ijimpeng.2016.04.014

Lai JZ, Zhu YY, Tan JM, 2016. Experiment and simulation of ultra-high performance concrete subjected to blast by embedded explosive. *Engineering Mechanics*, 33(5):193-199 (in Chinese). https://doi.org/10.6052/j.issn.1000-4750.2014.10.0874

Li HD, Xu S, 2011. Determination of energy consumption in the fracture plane of ultra high toughness cementitious composite with direct tension test. *Engineering Fracture Mechanics*, 78(9):1895-1905. https://doi.org/10.1016/j.engfracmech.2011.03.012

Li HD, Xu SL, 2016. Rate dependence of ultra high toughness cementitious composite under direct tension. *Journal of Zhejiang University-SCIENCE A (Applied Physics & Engineering)*, 17(6):417-426. https://doi.org/10.1631/jzus.A1600031

Li HY, Shi GY, 2016. A dynamic material model for rock materials under conditions of high confining pressures and high strain rates. *International Journal of Impact Engineering*, 89:38-48. https://doi.org/10.1016/j.ijimpeng.2015.11.004

Li QH, Zhao X, Xu SL, et al., 2016a. Influence of steel fiber on dynamic compressive behavior of hybrid fiber ultra high toughness cementitious composites at different strain rates. *Construction and Building Materials*, 125:490-500. https://doi.org/10.1016/j.conbuildmat.2016.08.066

Li QH, Huang BT, Zhou BM, et al., 2016b. Study on compression fatigue properties of ultra high toughness cementitious composites. *Journal of Building Structures*, 37(1):135-142 (in Chinese). https://doi.org/10.14006/j.jzjgxb.2016.01.015

Li Y, Liang XW, Liu ZJ, 2010. Behavior of high performance PVA fiber reinforced cement composites in triaxial compression. *Journal of Wuhan University of Technology*, 32(17):179-185.

Lin XS, 2018. Numerical simulation of blast responses of ultra-high performance fiber reinforced concrete panels with strain-rate effect. *Construction and Building Materials*, 176:371-382. https://doi.org/10.1016/j.conbuildmat.2018.05.066

Liu W, 2012. Experimental study on dynamic mechanical properties of ultra-high toughness cementitious composites. PhD Thesis, Dalian University of Technology, Dalian, China (in Chinese).

Liu Y, Ma AE, Huang FL, 2009. Numerical simulations of oblique-angle penetration by deformable projectiles into concrete targets. *International Journal of Impact Engineering*, 36(3):438-446. https://doi.org/10.1016/j.ijimpeng.2008.03.006

LSTC (Livermore Software Technology Corporation), 2012. LS-DYNA Keyword User's Manual, Volume I, Version 971. LSTC, Livermore, USA.

Malvar LJ, Crawford JE, Wesevich JW, et al., 1997. A plasticity concrete material model for DYNA3D. *International Journal of Impact Engineering*, 19(9-10):847-873. https://doi.org/10.1016/s0734-743x(97)00023-7

Mechtcherine V, Silva FDA, Butler M, et al., 2011. Behaviour of strain-hardening cement-based composites under high strain rates. *Journal of Advanced Concrete Technology*, 9(1):51-62. https://doi.org/10.3151/jact.9.51

Murray YD, 2007. User's Manual for LS-DYNA Concrete Material Model 159. Report No. FHWA-HRT-05-062, U.S. Department of Transportation, Federal Highway Administration, McLean, USA.

Pan JL, He JX, Wang LP, 2016. Experimental study on mechanical behaviors and failure criterion of engineered cementitious composites under biaxial compression. *Engineering Mechanics*, 33(6):186-193 (in Chinese). https://doi.org/10.6052/j.issn.1000-4750.2014.11.0969

Polanco-Loria M, Hopperstad OS, Børvik T, et al., 2008. Numerical predictions of ballistic limits for concrete slabs using a modified version of the HJC concrete model. *International Journal of Impact Engineering*, 35(5):290-303. https://doi.org/10.1016/j.ijimpeng.2007.03.001

Ranade R, Li VC, Heard WF, 2015. Tensile rate effects in high strength-high ductility concrete. *Cement and Concrete Research*, 68:94-104. https://doi.org/10.1016/j.cemconres.2014.11.005

Reinhardt HW, Cornelissen HAW, Hordijk DA, 1986. Tensile tests and failure analysis of concrete. *Journal of Structural Engineering*, 112(11):2462-2477. https://doi.org/10.1061/(asce)0733-9445(1986)112:11(2462)

Ren GM, Wu H, Fang Q, et al., 2016. Triaxial compressive behavior of UHPCC and applications in the projectile impact analyses. *Construction and Building Materials*, 113:1-14. https://doi.org/10.1016/j.conbuildmat.2016.02.227

Riedel W, Thoma K, Hiermaier S, et al., 1999. Penetration of reinforced concrete by BETA-B-500 numerical analysis using a new macroscopic concrete model for hydrocodes. Proceedings of the 9th International Symposium on the Interaction of the Effects of Munitions with Structures, p.315.

Schuler H, Mayrhofer C, Thoma K, 2006. Spall experiments for the measurement of the tensile strength and fracture energy of concrete at high strain rates. *International Journal of Impact Engineering*, 32(10):1635-1650. https://doi.org/10.1016/j.ijimpeng.2005.01.010

Soe KT, Zhang YX, Zhang LC, 2013. Impact resistance of hybrid-fiber engineered cementitious composite panels. *Composite Structures*, 104:320-330. https://doi.org/10.1016/j.compstruct.2013.01.029

Tu ZG, Lu Y, 2009. Evaluation of typical concrete material models used in hydrocodes for high dynamic response simulations. *International Journal of Impact Engineering*, 36(1):132-146. https://doi.org/10.1016/j.ijimpeng.2007.12.010

Wang SS, Le HTN, Poh LH, et al., 2016. Resistance of high-performance fiber-reinforced cement composites against high-velocity projectile impact. *International Journal of Impact Engineering*, 95:89-104. https://doi.org/10.1016/j.ijimpeng.2016.04.013

Weerheijm J, van Doormaal JCAM, 2007. Tensile failure of concrete at high loading rates: new test data on strength and fracture energy from instrumented spalling tests. *International Journal of Impact Engineering*, 34(3):609-626. https://doi.org/10.1016/j.ijimpeng.2006.01.005

Wen CG, 2015. Study on Mechanical Performance of Engineering Fiber Reinforced Cementitious Composites PVA-ECC. MS Thesis, Henan Polytechnic University, Jiaozuo, China (in Chinese).

Willam KJ, Warnke EP, 1975. Constitutive model for the triaxial behavior of concrete. Proceedings of International Association for Bridge and Structural Engineering, p.174.

Xu H, Wen HM, 2013. Semi-empirical equations for the dynamic strength enhancement of concrete-like materials. *International Journal of Impact Engineering*, 60:76-81. https://doi.org/10.1016/j.ijimpeng.2013.04.005

Xu H, Wen HM, 2016. A computational constitutive model for concrete subjected to dynamic loadings. *International Journal of Impact Engineering*, 91:116-125. https://doi.org/10.1016/j.ijimpeng.2016.01.003

Xu SL, Cai XR, 2008. Basic mechanical properties of ultra high toughness cementitious composite. *Journal of Hydraulic Engineering*, 39(S2):1055-1063 (in Chinese).

Xu SL, Li QH, 2010. Basic Application of Ultra High Toughness Cementitious Composites in Advanced Engineering Structures. Science Press, Beijing, China, p.5-6 (in Chinese).

Xu SL, Chen C, Li QH, et al., 2019. Numerical simulation on dynamic compressive behavior of ultra-high toughness cementitious-composites. *Engineering Mechanics*, 36(9):50-59 (in Chinese). https://doi.org/10.6052/j.issn.1000-4750.2018.03.0147

Yang EH, Li VC, 2014. Strain-rate effects on the tensile behavior of strain-hardening cementitious composites. *Construction and Building Materials*, 52:96-104. https://doi.org/10.1016/j.conbuildmat.2013.11.013

Zhao X, 2018. Experimental and Theoretical Study on the Dynamic Properties of Ultra High Toughness Cementitious. PhD Thesis, University of Zhejiang, Hangzhou, China (in Chinese).

Zhou JJ, Pan JL, Leung CKY, et al., 2013. Experimental study on mechanical behaviors of pseudo-ductile cementitious composites under biaxial compression. *Science China Technological Sciences*, 56(4):963-969. https://doi.org/10.1007/s11431-013-5174-9

中文概要

题　目：超高韧性水泥基复合材料动态本构关系

目　的：水泥基材料在动态荷载下会有压力相关性、应变率相关性、加载路径相关性以及应变软化等特性。根据现有水泥基材料的实验数据，本文旨在建立能够较为准确描述超高韧性水泥基复合材料在动态荷载作用下的显式动态本构模型，为超高韧性水泥基复合材料在防护工程中的应用提供科学依据。

创新点：1. 提出了一个连续、光滑和外凸的屈服面，并且该屈服面可以将拉压损伤分开考虑；2. 建立了可以反映超高韧性水泥基复合材料拉伸延性和多缝开裂现象的损伤方程；3. 将体积损伤引入到本文所提出的模型当中。

方　法：1. 将提出的模型嵌入到 LS-DYNSA 软件当中，并利用该模型模拟超高韧性水泥基复合材料在单轴拉伸/压缩、双轴压缩、三轴围压下的应力应变曲线，并与实验结果对比，验证模型的准确性；2. 利用该模型、HJC 模型和 K&C 模型预测不同应变率下超高韧性水泥基复合材料单轴拉伸/压缩下的应力应变曲线以及特定应变率下超高韧性水泥基复合材料的单轴拉伸、双轴拉伸和三轴

拉伸应力应变曲线，并通过对比实验，验证超高韧性水泥基复合材料动态本构模型在静态和动态加载条件下的正确性；3. 模拟在一定炸药埋置深度下超高韧性水泥基复合材料靶体的破坏形态和超高韧性水泥基复合材料靶体在弹速冲击下的破坏数据，并与实测结果进行对比，验证本文模型的准确性。

结　论： 1. 建立的超高韧性水泥基复合材料动态力学本构模型不仅考虑了压力相关性、应变软化、应变率效应和应力路径相关性，而且可以反映超高韧性水泥基复合材料的延性拉伸特性；2. 将所提模型嵌入 LS-DYNA 软件，可以模拟超高韧性水泥基复合材料在静态加载速率下的单轴拉伸/压缩、双轴压缩和三轴围压应力应变曲线，并且与实验结果接近且能更好地反映超高韧性水泥基复合材料的基本力学性能；3. 与 HJC 模型和 K&C 模型对比发现，只有所提模型可以全面而准确地描述不同应变率下超高韧性水泥基复合材料的应变率特性；4. 与实验结果对比显示，本文提出的本构模型相较于 HJC 模型可以更为准确地预测超高韧性水泥基复合材料靶体抗爆漏斗坑的大小、侵彻深度和裂纹扩展情况。

关键词： HJC 模型；超高韧性水泥基复合材料；动态本构关系；爆炸；侵彻；数值模拟